Progress In Electromagnetics Research M, Vol. 69, 51–60, 2018

Particle-In-Cell Simulation of a 5 kW Hall Thruster

Le Yang*, Lianjun Jia, Tianping Zhang, and Juanjuan Chen

Abstract—This paper aims to study the plasma discharge process of a 5 kW hall thruster developed by Lanzhou Institute of Physics and to provide the knowledge for implementing an improved thruster design. A 2D Particle-In-Cell (PIC) model is built, in which the electron-electron and electron-ion Coulomb collisions are included, in addition to the elastic, excitation, and ionization collisions between electrons and neutral atoms, and the elastic and charge-exchange collisions between ions and neutral atoms. Different Bohm diffusion coefficients are applied in different regions to simulate the Bohm diffusion. The deviation between the simulated and experimental results of the thruster performance is within 15%, validating the accuracy of the model indirectly. The discharge process including the transient and steady-state oscillations is well reproduced. The character of the plasma during different phase of the discharge process including the ion density and ionization rate is simulated and analyzed. Finally, the probable factor causing the anode erosion is determined.

1. INTRODUCTION

Evaluating the plasma discharge process and performance of hall thrusters by experiments is expensive and inefficient [1]. The numerical method plays an increasingly important role in understanding the micromechanism of the plasma discharge and helping to optimize thruster design. Among the numerical methods, hybrid method [2, 3] and Particle-In-Cell (PIC) method [4–6] are now being used widely. In the hybrid models, electrons are treated as continuous liquid, and neutral atoms and ions are treated as discrete particles. The wall potential is set according to the experiments or empirical formula [7], thus the sheath character cannot be studied. However, the sheath character is extremely important for predicting the plasma behavior and thruster performance, such as the sputtering of ceramic wall by ions and the life of hall thrusters. The wall potential is solved self-consistently in the PIC models. Thus, the PIC method has a higher accuracy.

Several problems have not been solved in the PIC method. Undoubtedly, an important issue is the electron diffusion across the magnetic field lines [8]. The collisions with other particles and the Bohm diffusion are two main factors affecting the electron diffusion. In many of the PIC models [9–11], the same Bohm diffusion coefficient is used in the whole region. However, experiments [8] have shown that the effect of Bohm diffusion is different in various regions. Thus, we applied different Bohm diffusion coefficients in different regions in this paper. In most of the present models, the Coulomb collisions between electrons and ions, and between electrons and electrons are excluded, whereas in this paper, the Coulomb collisions are included.

The focus of this paper is to demonstrate the ability of the built PIC model to study the plasma behavior in LHT-140 (shown in Fig. 1) and to provide knowledge for future optimization. In Section 2, we introduce the numerical methods used in this paper. In Section 3, the plasma discharge process and performance of the thruster are simulated and analyzed.

Received 17 April 2018, Accepted 29 May 2018, Scheduled 30 May 2018

* Corresponding author: Le Yang (yangle_23737@sina.com).

The authors are with the Science and Technology on Vacuum Technology and Physics Laboratory, Lanzhou Institute of Physics, Lanzhou 730000, China.

2. NUMERICAL METHODS

2.1. Simulation Region

The simulation region (shown in Fig. 2) consists of a discharge channel and near plume region. The length of the near plume region is 1.5 times that of the discharge channel, and the width is 4.5 times that of the discharge channel. The boundary of the discharge channel consists of metal anode wall, boron nitride ceramic wall, symmetric axis, and free space.

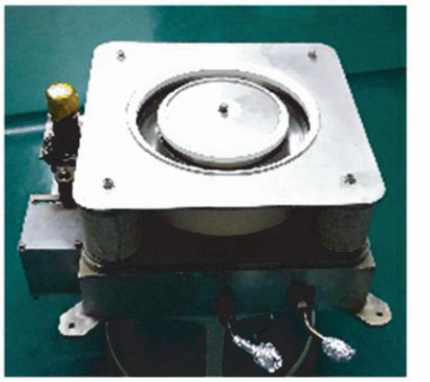

Figure 1. LHT-140 hall thruster.

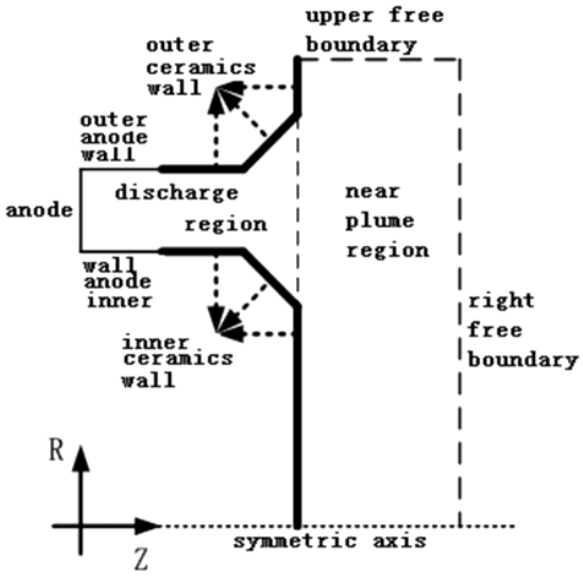

Figure 2. Simulation region.

2.2. Magnetic Field

The magnetic field produced by the plasma was less than that produced by the coils. Thus, only static magnetic field was considered. The static magnetic field (shown in Fig. 3) was pre-computed and dispersed to the grid points at the beginning of the simulation.

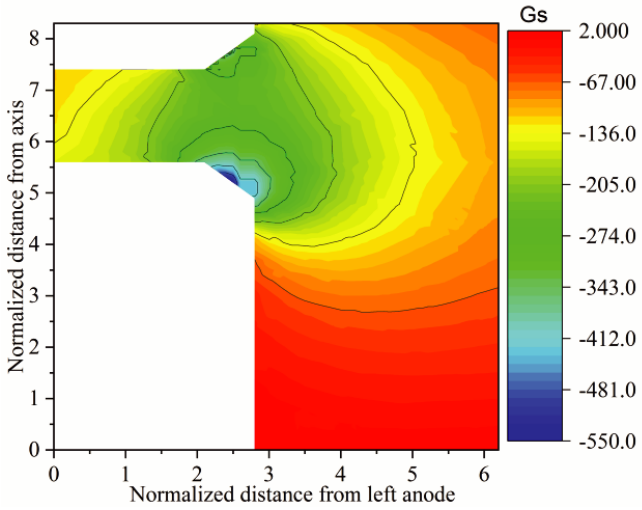

Figure 3. Radial magnetic field of LHT-140.

2.3. Potential and Electric Field Solving

The potential was acquired by solving the Poisson equation:

$$\nabla^2\phi = -\frac{\rho}{\varepsilon_0} \tag{1}$$

where ϕ is the electric potential, ρ the volume charge density in C/m^3, and ε_0 the vacuum permittivity.

The boundary conditions of the potential are as follows:

- At the anode surface, the potential is set to 300 V.
- At the symmetric axis, the normal electric field $E_\perp = 0$.
- At the free space boundary, the potential is set to 0 V.
- At the boron nitride ceramic wall surface, the boundary condition is [15]:

$$E_\perp^{plasma} - \varepsilon_{dieletric} E_\perp^{dielectric} = \frac{\sigma}{\varepsilon_0} \tag{2}$$

where $E_\perp^{plasma}$ is the normal electric field in the plasma near the boron nitride ceramic wall, $\varepsilon_{dieletric}$ the dielectric constant of boron nitride ceramics, $E_\perp^{dielectric}$ the normal electric field in the boron nitride ceramics, and σ the surface charge density, in C/m^2. For LHT-140 hall thruster, both in and outside the discharge channel, and $\varepsilon_{dieletric} E_\perp^{dielectric}$ the negligible compared with $E_\perp^{plasma}$. Thus, $\varepsilon_{dieletric} E_\perp^{dielectric}$ could be neglected, and formula (2) becomes:

$$E_\perp^{plasma} = \frac{\sigma}{\varepsilon_0} \tag{3}$$

The electric field was solved by Eqs. (4) and (5) [12]:

$$E_{x_{j,k}} = \frac{1}{3}\left(\frac{1}{2}\frac{\phi_{k+1,j-1} - \phi_{k+1,j+1}}{2x} + \frac{\phi_{k,j-1} - \phi_{k,j+1}}{x} + \frac{1}{2}\frac{\phi_{k-1,j-1} - \phi_{k-1,j+1}}{2x} \right) \tag{4}$$

$$E_{y_{j,k}} = \frac{1}{3}\left(\frac{1}{2}\frac{\phi_{k-1,j-1} - \phi_{k+1,j-1}}{2x} + \frac{\phi_{k-1,j} - \phi_{k+1,j}}{x} + \frac{1}{2}\frac{\phi_{k-1,j+1} - \phi_{k+1,j+1}}{2x} \right) \tag{5}$$

where $E_{x_{j,k}}$ and $E_{y_{j,k}}$ are the electric field on the grid point (j,k) in the x and y directions respectively; and $\phi_{k+1,j-1}$, $\phi_{k+1,j+1}$, $\phi_{k,j-1}$, $\phi_{k,j+1}$, $\phi_{k-1,j-1}$, $\phi_{k-1,j+1}$, $\phi_{k-1,j}$ and $\phi_{k+1,j}$ are the electric potential on the grid points around (k,j); x is the width of the square grid.

2.4. Electron Diffusion

The main factors determining the electron diffusion are the collisions with other particles, collisions with the wall (near-wall conduction), and the Bohm diffusion. For the collisions with other particles, the Coulomb collisions are always excluded. In this paper, we modeled the Coulomb collisions as follows:

$$\nu_{ei} = n_i Q_{ei} |v_e| \tag{6}$$

$$\nu_{ee} = n_e Q_{ee} |v_e| \tag{7}$$

where n_i is the density of ions, n_e the density of electrons, and v_e the electron velocity. The collision section was calculated as follows:

$$Q_{ei} = \frac{6.5 \times 10^{-14}}{E_{eV}^2} \ln\Lambda \text{cm}^2 \tag{8}$$

$$Q_{ee} = \frac{4.34 \times 10^{-14}}{T_e^2} \ln\Lambda \text{cm}^2 \tag{9}$$

where E_{eV} is the electron kinetic energy, T_e the electron temperature, and $\ln\Lambda$ the Coulomb logarithm. For the collisions with the ceramic wall, when an primary electron collides the ceramic wall, the number of secondary electrons emitted from the ceramic wall is [13]:

$$\delta_w = \Gamma\left[2 + b\right] a T_e^b \tag{10}$$

Γ is gamma function, T_e the electron temperature, $a = 0.123$, and $b = 0.528$. δ_w consists of an integral part and a decimal part, and needs to be converted to an integer N_s in the simulation as follows:

$$N_s = \lceil \delta_w \rceil + \{R_f < (\delta_w - \lceil \delta_w \rceil)\} \tag{11}$$

$\lceil \delta_w \rceil$ means rounding δ_w down to an integer. R_f is a random number between 0 and 1. If $R_f < (\delta_w - \lceil \delta_w \rceil)$, $N_s = \lceil \delta_w \rceil + 1$, and the primary electron is reflected back into the plasma as a secondary electron. Otherwise, $N_s = \lceil \delta_w \rceil$ and the primary electron accumulates on the ceramic wall. For the Bohm diffusion, a virtual collision "Bohm collision" is introduced to model it. The Bohm collision frequency is

$$\nu_{Bohm} = \frac{w_{ce}}{\alpha} \tag{12}$$

where w_{ce} is the electron cyclotron frequency, and α is the Bohm diffusion coefficient. We assumed that $\alpha = 200$ in the ionization region (between the ceramic wall), $\alpha = 128$ in the near-anode region, and $\alpha = 64$ in the near-plume region. Qualitatively similar profiles have been obtained in previous experiment [14] and applied in Reference [4].

2.5. Sheath Correction

Usually, the ions are accelerated artificially to shorten the time of convergence of the model by reducing the mass by a factor $f = M_i/M_i'$. M_i is the real mass of the ion, and M_i' is the artificial ion mass which is used in the model. When the artificial ion mass M_i' is applied, the theoretical sheath magnitude $\Delta\phi^{\text{real}}$ with the real ion mass will be reduced. Thus, the computational sheath magnitude $\Delta\phi^{\text{comp}}$ with the artificial ion mass in the simulation needs to be corrected. When an electron collided with the ceramic wall, we compared its energy, E_e, to the difference between theoretical and computational sheath magnitudes, as described below:

$$\Delta\varphi = -\left(K\Delta\phi^{\text{real}} - K\Delta\phi^{\text{comp}}\right) \approx \frac{K}{2}\ln(f)\frac{kT_e}{e} \tag{13}$$

If $E_e > e \times \Delta\varphi$, then a real collision occurs, and the collision will be treated by the secondary electron emission model. If $E_e < e \times \Delta\varphi$, then a real collision does not occur, and the electron will be reflected back to the plasma. Then, we will find a good candidate with energy $E_e > e \times \Delta\varphi$ near the collision position to replace the rejected electron. K is the sheath potential correction coefficient, which is set to 1 at the beginning of the simulation. If we cannot find a good candidate, then K is decreased by multiplying it by 0.95.

2.6. Cathode Modeling

The cathode is modeled by injecting electrons from the upper free boundary with 0.1 eV of kinetic energy. The number of electrons injected in each time step is determined by current balance.

$$I_c = I_{cb} + I_{cd} \tag{14}$$

where I_c is the cathode current, I_{cb} the current getting into the plume, and I_{cd} the current getting into the simulation region. Cathode current getting into the discharge region I_{cd}, ion current leaving from the free boundary I_b^+, and electron current leaving from the free boundary I_{az} satisfy the following constraints:

$$I_{cd} = I_c - I_b^+ + I_{az} \tag{15}$$

From formula (15), the number of electrons injected in each time step could be determined.

3. RESULTS AND DISCUSSION

3.1. Performance Simulation

The performance of LHT-140, including thrust, anode specific impulse and anode efficiency, was tested in the vacuum chamber TS-7 (shown in Fig. 4) with a diameter of 3.8 m and a length of 8.5 m, when the discharge voltage ranged from 300 V to 800 V, and the anode propellant mass flow rate ranged from

2.5 mg/s to 5.4 mg/s. Anode specific impulse is a measure of thrust efficiency of the anode and is defined as the ratio of the thrust to the rate of anode propellant consumption. Anode efficiency is a measure of energy conversion efficiency of the anode and is defined as the kinetic power of the ion beam divided by the discharge power.

Figure 5 shows the comparison between experimental and simulated results of the performance. The simulated value of the discharge current was less than the test value by 5% to 13%, and the simulated

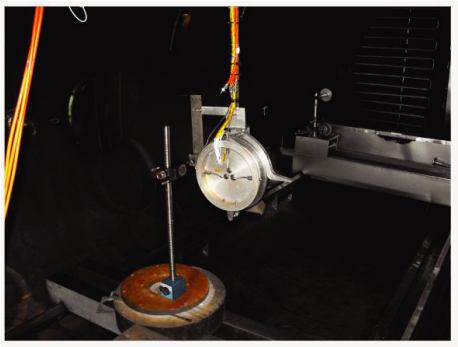

Figure 4. Performance test of LHT-140.

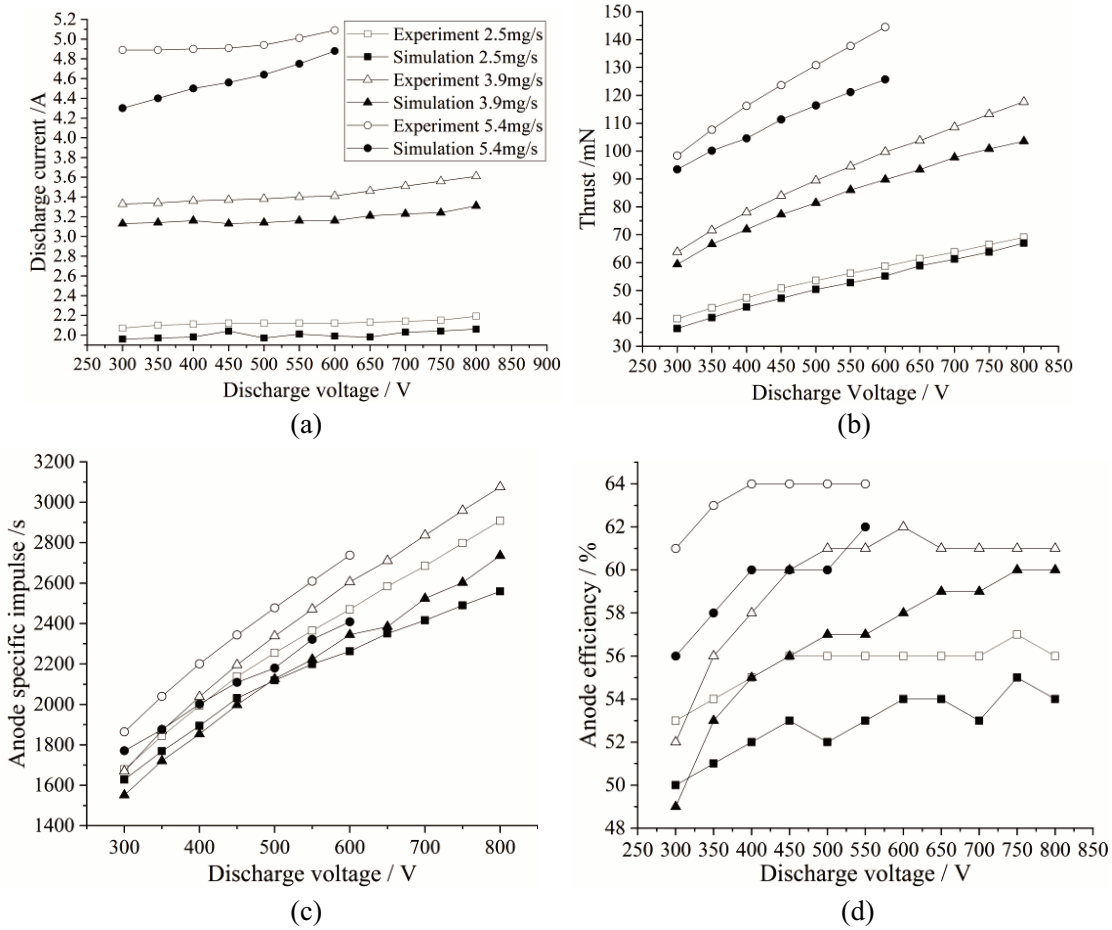

Figure 5. Comparisons between experimental and numerical performance results. (a) Discharge current. (b) Thrust. (c) Anode specific impulse. (d) Anode efficiency.

value of the thrust was less than the test value by 3% to 12%. In all cases, the deviation between the experimental and simulated results of the performance was within 15%.

3.2. Transient Oscillation Stage

Figure 6 presents the change in the number of macroparticles with time when the discharge voltage was 300 V and the propellant mass flow rate was 10 mg/s. After the discharge begins, the number reached the maximum rapidly at approximately 20 μs and then fell into periodic oscillation. The rapid rising process is called transient oscillation. The change of current with time was similar to that of the number of macroparticles, as shown in Fig. 7. At approximately 20 μs, the discharge current reached the maximum value of 25 A, which was twice that of the steady-state value.

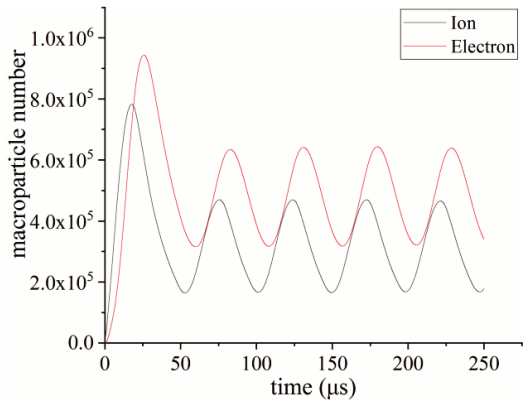

Figure 6. Time history of macro-particle number.

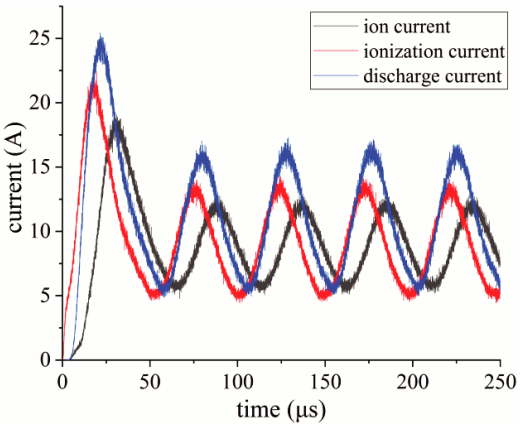

Figure 7. Time history of current.

To understand the physical process during the transient oscillation, ion density values at 1, 10, 25, and 50 μs after the beginning of discharge were simulated and analyzed. As shown in Fig. 8(a), before 1 μs, electrons entered the near plume region from the upper free boundary and performed the hall drift under the confinement of the magnetic field. After a collision with a neutral, the hall drift was broken and electrons moved toward the anode under the action of axial electric field. The neutral density was relatively small. Thus, the probability of collisions between electrons and neutral atoms was relative small. Therefore, electrons were mainly distributed in the near plume region. The ionization rate and ion density were small due to the low neutral density and small electron kinetic energy. The produced low-density plasma creates conditions for the electrons moving deep into the discharge channel.

From 1 μs to 10 μs, as the electrons moved upstream where the neutral density was relatively large and their kinetic energy increased, the ion density and ionization rate increased, and the main ionization region also moves upstream. From 10 μs to 25 μs, the main ionization region came to the position where it was located during the steady-state oscillation, approximately 1.5 normalized distance upstream of the channel exit. From 25 μs to 50 μs, the ion density decreased to the steady-state value as the neutral density decreased due to excessive ionization, which indicated that the steady-state oscillation started.

3.3. Steady State Oscillation Stage

The steady state oscillation after the transient oscillation is the so-called breathing-mode oscillation [15–17], which is caused by a periodic depletion and replenishment of neutrals near the exit. In this section, the steady state plasma character is simulated and analyzed. First, the influence of the Bohm diffusion coefficient is studied by using the one-dimensional parameter distributions on the centerline of the channel. Second, the discharge character of the plasma during different stages of the oscillation is studied by using the two-dimensional distributions of ionization rate and ion density.

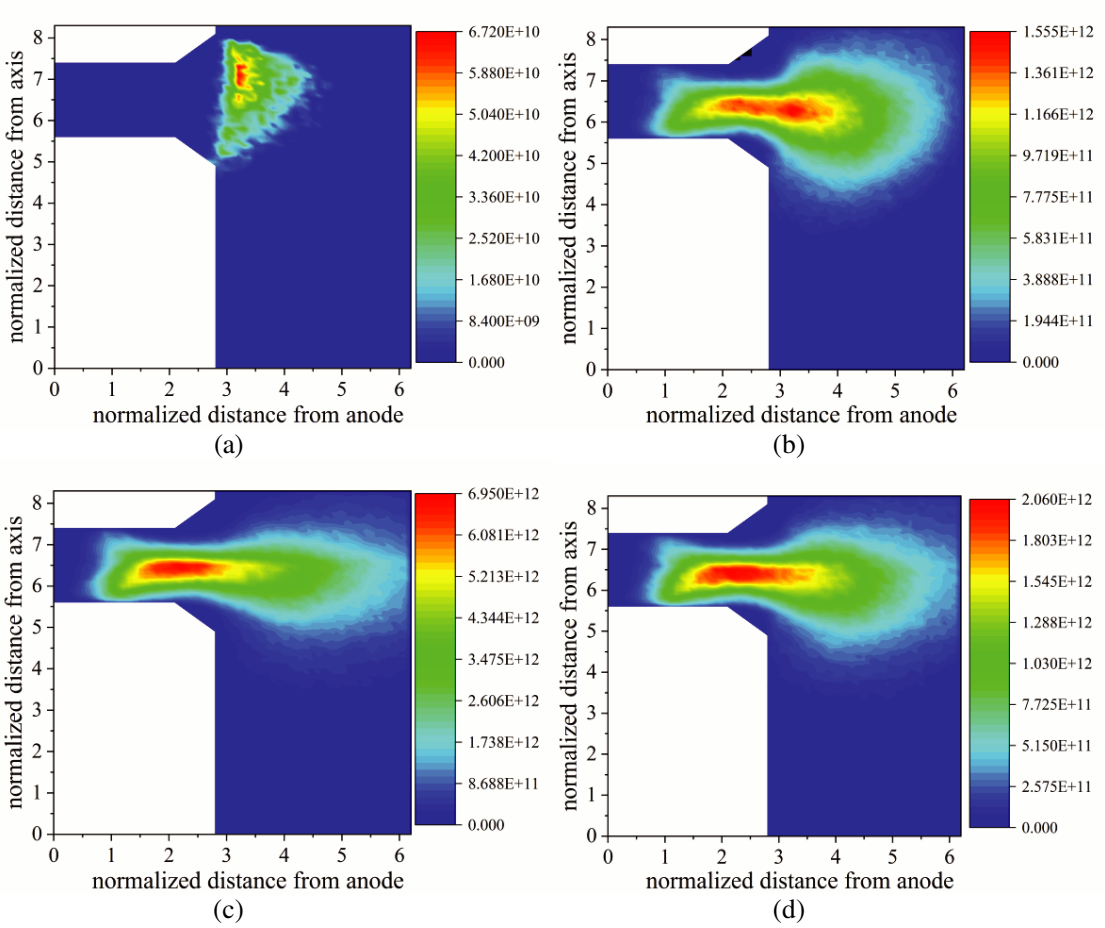

Figure 8. Ion density at different stages of the transient oscillation (cm^{-3}). (a) 1 μs. (b) 10 μs. (c) 25 μs. (d) 50 μs.

Figures 9(a) and (b) present the distributions of magnetic field, ionization rate and electron kinetic energy on the centerline of the channel with and without the Bohm diffusion. The horizontal ordinate is the normalized distance from the anode. The anode is located at $z/L = 0$ and $z/L = 1$ which means the channel exit. The longitudinal coordinates are the normalized values of the plasma parameters divided by the maximum value of each. In Fig. 9(a), when the Bohm diffusion was modeled, the position of the maximum electron kinetic energy was located upstream of the position of the maximum magnetic field. This observation was in accordance with the past study [18]. In Fig. 9(b), when the Bohm diffusion was excluded, the position of the maximum electron kinetic energy was located downstream of the position of the maximum magnetic field. Moreover, Fig. 9(a) indicates that the ionization region is located between the location of the maximum magnetic field and 50% of the maximum magnetic field.

The influence of the Bohm diffusion coefficients on the plasma character is studied in four cases shown in Table 1.

Figure 10 denotes that the influence of the Bohm diffusion coefficients on the potential is very small in the near anode and ionization region. In the plume region, from 3 to 5 normalized distances, the potential is larger when the Bohm diffusion coefficients are larger. Besides, in any case, the large potential drop is located between the ceramic wall, where the electric field is large due to the low electron conductivity caused by the strong magnetic field. Furthermore, Fig. 11 demonstrates that the electron kinetic energy decreases and its peak moves toward the anode as the Bohm diffusion coefficients increase.

The average values of the ion density and ionization rate during the periodic oscillation in 100 time steps are shown in Fig. 12 and Fig. 13. Those values at the point P1 on the channel centerline (the

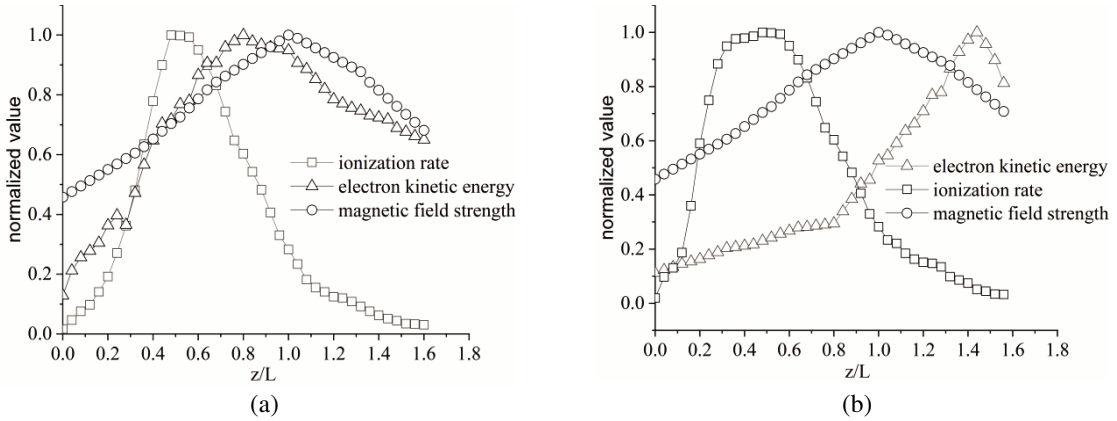

Figure 9. Distributions of the plasma parameters on the discharge channel centerline. (a) With Bohm diffusion. (b) Without Bohm diffusion.

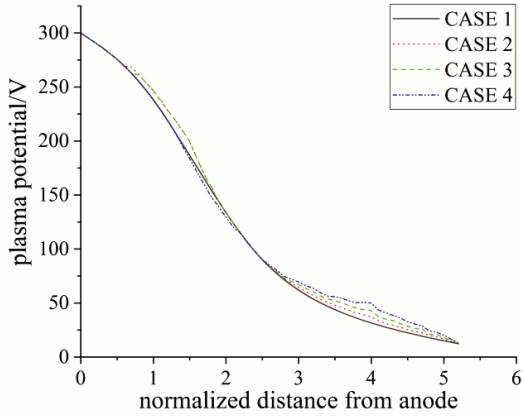

Figure 10. Distributions of plasma potential with different Bohm diffusion coefficients.

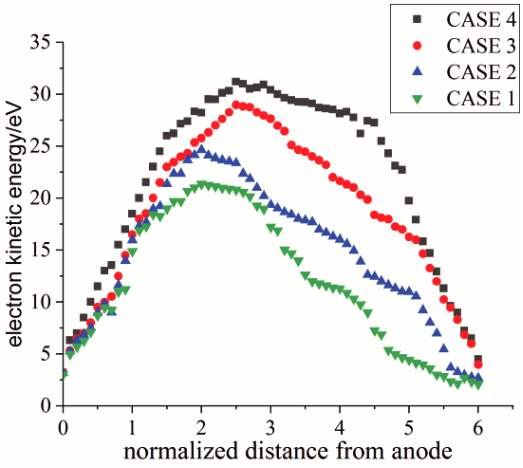

Figure 11. Distributions of electron kinetic energy with different Bohm diffusion coefficients.

normalized distances from the axis is 6.5), which was 1.5 normalized distances from the anode, were sampled during four stages of the oscillation cycle of the discharge current, Rising, Maximum, Falling and Minimum stages. Clearly, the trends of the ion density and ionization rate were in accordance with that of the discharge current. The ion density at P1 rose to $3.5 \times 10^{12}\,\mathrm{cm}^{-3}$ at the Rising stage, reached the maximum value of $3.9 \times 10^{12}\,\mathrm{cm}^{-3}$ at the Maximum stage, fell to $2.2 \times 10^{12}\,\mathrm{cm}^{-3}$ at the Falling stage, and finally reached the minimum value of $2.1 \times 10^{12}\,\mathrm{cm}^{-3}$ at the Minimum stage. The ionization rate at P1 rose to $2.9 \times 10^{17}\,\mathrm{cm}^{-3}\mathrm{s}^{-1}$ at the Rising stage, reached the maximum value of $4.7 \times 10^{17}\,\mathrm{cm}^{-3}\mathrm{s}^{-1}$ at the Maximum stage, fell to $2.9 \times 10^{17}\,\mathrm{cm}^{-3}\mathrm{s}^{-1}$ at the Falling stage, and finally

Table 1. Four cases of the Bohm diffusion coefficients.

CASE / REGION	CASE 1	CASE 2	CASE 3	CASE 4
ionization region	200	250	300	350
near anode region	128	160	192	224
plume region	64	80	96	112

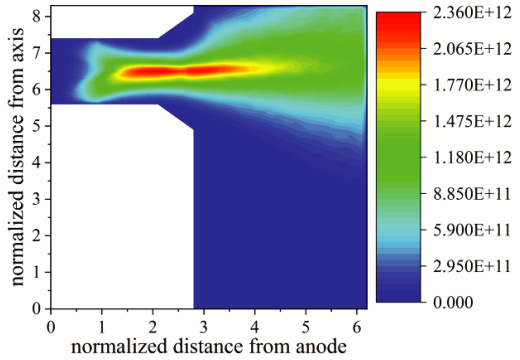

Figure 12. Average values of ion density (cm^{-3}).

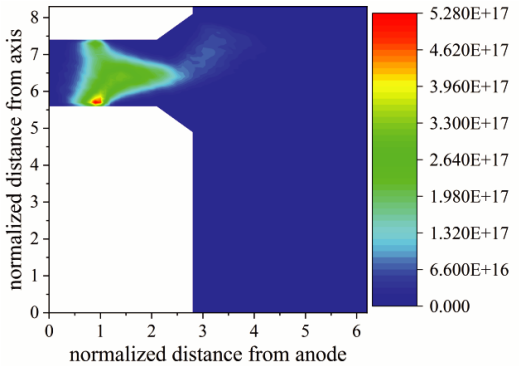

Figure 13. Average values of ionization rate ($cm^{-3}s^{-1}$).

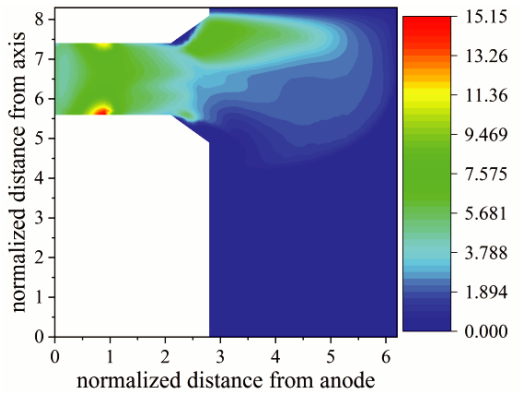

Figure 14. Electron temperature T_e (eV).

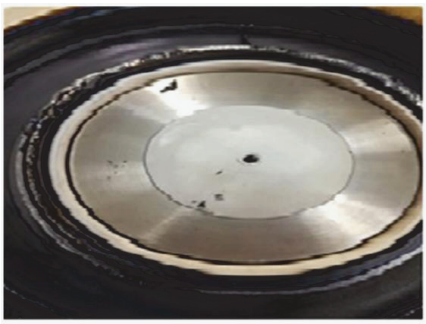

Figure 15. Eroded anode wall of LHT-140.

reached the minimum value of $2.2 \times 10^{17}\,cm^{-3}s^{-1}$ at the Minimum stage.

The electron temperature distribution, shown in Fig. 14, indicates that the high temperature electrons are mainly located at the position, where the anode wall is in contact with the ceramic wall, and this is also the place where the anode eroded (shown in Fig. 15). Thus, the anode erosion is probably caused mainly by the high-temperature electrons.

4. CONCLUSIONS

The built model can reproduce the process of the plasma discharge, consisting of a transient oscillation and a steady-state oscillation. The model can also estimate the performance of LHT-140 accurately. The deviation between the simulated and experimental results is within 15%. The simulation results show that Bohm diffusion has a great influence on electron diffusion, and the electron character could be modeled accurately only with the Bohm diffusion. The values of Bohm diffusion coefficients affect the plasma character, such as the plasma potential and electron energy, but will not change the basic physical process of plasma discharge. Notably, the simulation shows that the anode erosion is probably caused by the high temperature electrons.

REFERENCES

1. Huang, W. and A. D. Gallimore, "A low-cost optical approach to evaluate the life time of hall thruster discharge channel," *48th AIAA/ASME/SAE/ASEE Joint Propulsion Conference & Exhibit*, AIAA-2012-4035, Atlanta, Georgia, July 30–August 1, 2012.

2. Mikellides, I. G. and I. Katz, "Numerical simulations of Hall-effect plasma accelerators on a magnetic-field-aligned mesh," *Phys. Rev. E*, Vol. 86, 046703, 2012.
3. Parra, F. I., E. Ahedo, J. M. Fife, and M. Martinez-Sanchez, "A two-dimensional hybrid model of the Hall thruster discharge," *J. Appl. Phys.*, Vol. 100, 023304, 2006.
4. Szabo, J., N. Warner, M. Martinez-Sanchez, and O. Batishchev, "Full particle-in-cell simulation methodology for axisymmetric hall effect thrusters," *Journal of Propulsion and Power*, Vol. 30, No. 1, 197–208, 2015.
5. Yokota, S., K. Komurasaki, and Y. Arakawa, " Plasma density fluctuation inside a hollow anode in an anode-layer Hall thruster," *AIAA Meeting Papers on DISC-CD ROM Edition; Joint Propulsion Conference & Exhibit AIAA*, AIAA Paper 2006-5170, 2006.
6. Takao, Y., H. Koizumi, K. Komurasaki, K. Eriguchi, and K. Ono, "Three-dimen-sional particle-in-cell simulation of a miniature plasma source for a microwave discharge ion thruster," *Plasma Sources Sci. Technol.*, Vol. 23, 064004, 2014.
7. Hofer, R. R., I. Katz, I. G. Mikellides, D. M. Goebel, and K. K. Jameson, "Efficacy of electron mobility models in hybrid-PIC Hall thruster simulations," *44th AIAA/ASME/SAE/ASEE Joint Propulsion Conference & Exhibit*, AIAA 2008-4924, Hartford, CT, July 21–23, 2008.
8. Meezan, N. B., W. A. Hargus, and M. A. Cappelli, "Anomalous electron mobility in a coaxial hall discharge plasma," *Phys. Rev. E*, Vol. 63, 026410, 2001.
9. Ahedo, E., J. M. Gallardo, and M. Martinez-Sanchez, "Model of the plasma discharge in a Hall thruster with heat conduction," *Physics of Plasmas*, Vol. 9, No. 9, 4061–4070, 2002.
10. Cho, S., K. Komurasaki, and Y. Arakawa, "Kinetic particle simulation of discharge and wall erosion of a Hall thruster," *Physics of Plasmas*, Vol. 20, No. 6, 063501, 2013.
11. Cho, S., H. Watanabe, and K. Kubota, "Study of electron transport in a Hall thruster by axial-radial fully kinetic particle simulation," *Physics of Plasmas*, Vol. 22, 103523, 2015.
12. Birdsall, C. K. and A. B. Langdon, *Plasma Physics via Computer Simulation*, Institute of Physics Publishing, Bristol and Philadelphia, 1991.
13. Hofer, R. R. and I. G. Mikellides, "Wall sheath and electron mobility modeling in hybrid-PIC hall thruster simulations," *43rd AIAA/ASME/SAE/ASEE Joint Propulsion Conference & Exhibit*, AIAA-2007-52-67, Cincinnati, OH, July 8–11, 2007.
14. Meezan, N., W. Hargus, and M. Cappelli, "Anomalous electron mobility in a coaxial hall discharge plasma," *Physical Review E*, Vol. 63, No. 2, Paper 026410, 2001.
15. Choueiri, E. Y., "Plasma oscillations in Hall thrusters," *Physics of Plasmas*, Vol. 8, No. 4, 1354644, 2001.
16. Boeul, J. P. and L. Garrigues, "Low frequency oscillation in a stationary plasma thruster," *Journal of Applied Physics*, Vol. 84, No. 7, 3541–3554, 1998.
17. Barral, S. and E. Ahedo, "Low-frequency model of breathing oscillations in Hall discharges," *Physical Review E*, Vol. 79, 046401, 2009.
18. Haas, J. M. and A. D. Gallimore, "Internal plasma potential profiles in a laboratory-model Hall thruster," *Physics of Plasmas*, Vol. 8, 652, 2001.